

Full-stroke Static and Dynamic Analysis of High-power Piezoelectric Actuators

RADU POMIRLEANU AND VICTOR GIURGIUTIU*

Department of Mechanical Engineering, University of South Carolina, Columbia, SC 29208, USA

ABSTRACT: A method for characterizing smart materials actuators in full-stroke static and low frequency dynamic regimes is presented. At first, static and dynamic linear models of the piezoelectric actuator response under electro-mechanical excitation are discussed. Then, a thorough static and dynamic experimental characterization on a typical large-stroke piezoelectric actuator is performed. The measurements indicated a strong dependence of the actuator stiffness and piezoelectric properties on the electromechanical loading. The comparison of the model with the measured behavior is performed and the material coefficients are tuned to locally match the observed nonlinear behavior. The comparison also allows the identification of key parameters of the induced-strain actuator model. These parameters are necessary for design optimization towards maximum mechanical energy output and minimum electrical power input. The paper provides useful basic data for the design of actuation systems incorporating active materials actuators.

Key Words: PZT, piezoelectric, active materials, actuators, smart materials, induced strain, blocked force, full-stroke, high power, piezoelectric stack

INTRODUCTION

State of the Art in Piezoelectric Actuators Modeling and Characterization

CONVENTIONAL modeling of piezoelectric material response assumes the piezoelectric material as a continuum, described by constitutive equations in terms of three material-properties tensors (the compliance, s_{ijkl} , the piezoelectric, d_{ijk} , and the dielectric permittivity, ϵ_{ij}) and four field quantities (strain, S_{ij} , stress, T_{kl} , electric field, E_k , and electric displacement, D_i):

$$S_{ij} = s_{ijkl}^E T_{kl} + d_{kij} E_k \quad D_i = d_{ikl} T_{kl} + \epsilon_{ik}^T E_k \quad (1)$$

Nonetheless, this electro-mechanical linear model can accurately describe only a fraction of the full operating range of induced-strain actuators. Full-stroke operation is significantly nonlinear. Hence, the prediction of the maximum design force and the displacement as well as the maximum available mechanical energy and the required electrical energy of an active material actuator can be only approximately estimated using the linear constitutive equations.

Krueger and Berlincourt (1961) characterized the nonlinear behavior of piezoelectric materials under high-stress conditions for naval transducer applications by relating the deviations from linear behavior to

macroscopic quantities such as dielectric permittivity, piezoelectric coefficient, loss factor, and coupling coefficients. Although exclusively based on macroscopic effects, this approach was useful in recognizing the basic differences in the responses of hard and soft PZTs. These early experiments showed that the tensorial material properties varied significantly with the electro-mechanical boundary conditions and that time-history effects are important. A strong dependence of dielectric permittivity on stress and applied AC field amplitude was also observed (Krueger, 1967, 1968; Brennan and McGowan, 1997; Jordan et al., 2000).

Attempts to understand and explain the nonlinear piezoelectric response considered the microstructure behavior through domain switching under high electro-mechanical loads, where the domains inside a piezoelectric material crystal are defined as regions with the same direction of the remnant polarization vector (Lynch, 1996). Carefully conducted experiments on various doped PZT ceramics have been pursued to determine the polarization switching behavior under high electric fields and compressive stresses (Zhang et al., 1997; Fan et al., 1999; Ching-Yu and Hagood, 2000; Lin and Hagood, 2000; Yang et al., 2000).

Several modeling attempts have tried to bridge the gap between the micro-mechanics of the crystal structure and the macroscopic properties of piezoceramics under high electro-mechanical driving conditions (Chen et al., 1997; Fan et al., 1999; Hwang and McMeeking, 2000; Huber and Fleck, 2001). Such modeling efforts have been confined to the analysis of bulk piezoelectric material

*Author to whom correspondence should be addressed. E-mail: victorg@sc.edu

subjected to precisely known electro-mechanical excitation, and under negligible boundary conditions influence. However, in the case of stacked piezoelectric actuators consisting of hundreds of thin layers, the electro-mechanical boundary conditions for every layer are insufficiently known and difficult to define. Consequently, the characterization of actual stack actuators has been, so far, phenomenological through measurement and data fitting rather than micromechanical modeling. Straub and Merkley (1995), Lee and Chopra (1999), Mitrovic et al. (1999, 2000), Straub et al. (1999), Pan et al. (2000) obtained essential design information about the mechanical stiffness, energy density, load amplitude, temperature effects, and durability. These tests used various methods for external load application, such as dead weight (Lee and Chopra, 1999), MTS machine (Mitrovic et al., 1999, 2000), variable impedance through a variable-stiffness spring (Straub et al., 1999), or constant stiffness spring mounted in series with the smart material actuator (Pan et al., 2000).

Present Investigation

The present study took a design-oriented approach to model and characterize the static and dynamic behavior of piezoelectric actuators. A high stroke/ high force piezoelectric actuator (PiezoSystems Jena PAHL 120/20) was modeled using quasi-linear models. Systematic experiments were performed to characterize the actuator behavior over the full range of external load and excitation voltage. The linear piezoelectric model was found capable to provide a first-order approximation for the actuator behavior only under no-load conditions. The measurements performed under increasing external load showed increasing nonlinearity associated with the intrinsic material response under high mechanical stresses. For each load–voltage–frequency condition, a quasi-linear model was tuned to the experimental data, revealing consistent coefficients patterns in terms of frequency, prestress level and applied electric field. The experimental observations were found to be consistent with existing microstructure theories relating the macroscopic actuator behavior to the polarization domains dynamics inside the active material ceramic. The actuator characterization results obtained in this study are presented in a form suitable for direct application to induced-strain actuation design.

STATIC AND DYNAMIC MODELING OF PIEZOELECTRIC STACK ACTUATORS

Piezoelectric Actuators Modeling

The PiezoSystems Jena piezoelectric actuator PAHL 120/20 (Figure 1a) consists of an active material stack

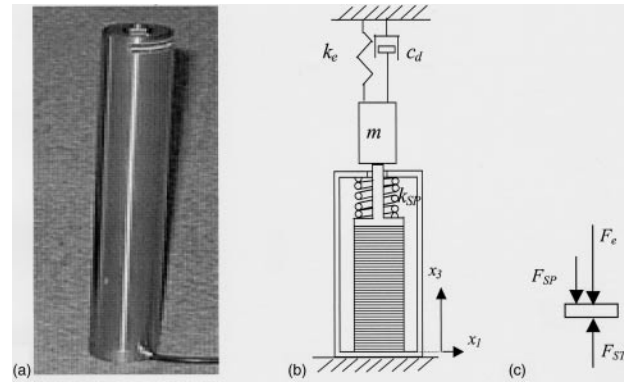


Figure 1. (a) Piezoelectric stack actuator PAHL 120/20; (b) idealized actuator and external structure; (c) free-body diagram for the pushing rod.

Table 1. PiezoSystems Jena actuator properties.

Actuator Properties and Dimensions	
Maximum displacement (μm)	120
Voltage range (V)	– 10 to 180
Actuator internal stiffness (kN/mm)	30
Maximum tensile force (N)	350
Maximum blocked force (N)	3500
Capacitance (for small strength electrical fields) (μF)	42
Resonance frequency (kHz)	5
Length (mm)	126
Diameter (mm)	20
Piezoelectric coefficient d_{33} ($10^{-12} \times \text{m/V}$)	700
Compliance s_{33}^E ($10^{-12} \times \text{m}^2/\text{N}$)	20.8
Coupling factor κ_{33}	0.65
Stack length L (mm)	118
Stack area A (mm^2)	64
Layer thickness t (mm)	0.1

prestressed to $F_0 = 350$ N by an internal spring inside a steel casing (Figure 1b). The mechanical prestress is needed to prevent tensile stresses in the stack during static and dynamic applications. The space between the steel casing and the piezoelectric stack is filled with epoxy resin to protect the stack from shocks. The piezoelectric stack transmits force through a steel push-rod. The piezoelectric material used is a soft PZT, with the manufacturer provided characteristics shown in Table 1.

The linear piezoelectric equations (ANSI/IEEE Std. 176, 1987) were used to describe the active material behavior by simplifying to the case where only the 3-direction effects (i.e. in the direction of remnant polarization) are retained, and the effects that take place in the plane perpendicular to the 3-direction (e.g. interaction with the resin layer, nonuniform distribution of the electric field through the active material, etc.) are neglected. Consequently:

$$S_3 = s_{33}^{(E)} T_3 + d_{33} E_3 \quad D_3 = d_{33} T_3 + \varepsilon_3^{(T)} E_3 \quad (2)$$

STATIC MODEL

The static model assumes that the application of electrical and mechanical loads to the actuator constitutes an equilibrium process and, consequently, the static loads super-position can be applied. The loading of the active material stack was considered applied in 3 steps:

- The prestress force F_0 is applied through the compression of the internal spring k_{SP} against the casing. During this process, both the stack and the internal spring are compressed;
- The force $F_e^{(b)}$ is applied by compressing the external spring k_e against an external support. During this process, the stack and the external spring are compressed, while the internal spring expands;
- A positive voltage V is applied. The stack expands, remaining in compression.

The piezoelectric and stiffness properties of the stack are assumed to remain constant throughout this 3-step process. After the first step, the stack displacement, strain, and stress are:

$$\Delta L^{(a)} = \frac{L}{k_{ST}^{(E)}} \quad S_3^{(a)} = \frac{1}{L} k_{ST}^{(E)} F_0 \quad T_3^{(a)} = \frac{F_0}{A} \quad (3)$$

The stack stiffness, $k_{ST}^{(E)}$, can be evaluated using the closed-circuit material compliance value, $s_{33}^{(E)}$, reported by the manufacturer:

$$k_{ST}^{(E)} = \frac{A}{s_{33}^{(E)} L} \quad (4)$$

During step (b), the application of the external mechanical load F_e (Figure 1(c)) leads to:

$$F_{ST}^{(b)} = F_e^{(b)} + F_{SP}^{(b)} \quad (5)$$

Consequently, the displacement increment from state (a) to state (b), the strain and the stress at the end of step (b) are:

$$\Delta L^{(b)} = \frac{F_e^{(b)}}{k_{ST}^{(E)} + k_{SP}}, \quad S_3^{(b)} = \frac{(1 + (k_{SP}/k_{ST}^{(E)}))F_0 + F_e^{(b)}}{L(k_{ST}^{(E)} + k_{SP})},$$

$$T_3^{(b)} = \frac{(1 + (k_{SP}/k_{ST}^{(E)}))F_0 + F_e^{(b)}}{A(1 + (k_{SP}/k_{ST}^{(E)}))} \quad (6)$$

The application of the voltage in step (c) does not change the free-body diagram (Figure 1c), but adds a positive stack displacement, i.e.:

$$\Delta L^{(c)} = \frac{Ad_{33}}{ts_{33}^{(E)}} \frac{V}{k_e + k_{SP} + k_{ST}^{(E)}} \quad (7)$$

The corresponding strain and stress are:

$$S_3^{(c)} = \frac{(1 + (k_{SP}/k_{ST}^{(E)}))F_0 + F_e^{(b)}}{(k_{ST}^{(E)} + k_{SP})L} + \frac{d_{33}}{t} k_{ST}^{(E)} \frac{V}{k_e + k_{SP} + k_{ST}^{(E)}}$$

$$T_3^{(c)} = \frac{F_0}{A} + \frac{F_e^{(b)}}{A} \cdot \frac{k_{ST}^{(E)}}{k_{ST}^{(E)} + k_{SP}} - \frac{d_{33} \cdot V}{t \cdot s_{33}^{(E)}} \frac{k_e + k_{SP}}{k_{ST}^{(E)} + k_e + k_{SP}} \quad (8)$$

Hence, the external force $F_e^{(c)}$, which can be directly compared with the experimental data, results as:

$$F_e^{(c)} = F_e^{(b)} - A \frac{d_{33} \cdot V}{t \cdot s_{33}^{(E)}} \frac{k_e}{k_e + k_{SP} + k_{ST}^{(E)}} \quad (9)$$

DYNAMIC LINEAR MODEL

The dynamic model describes the response of the piezoelectric actuator under in-phase electro-mechanical loading. The wave equation can model the response of an elastic medium under harmonic excitation. This approach, proposed by Ikeda (1990) and Liang et al. (1994) in conjunction with thin PZT wafers modeling, was later expanded to piezoelectric and magnetostrictive actuators by Giurgiutiu et al. (1994), Giurgiutiu and Rogers (1996), and Ackerman et al. (1996). The one-dimensional wave equation is:

$$\frac{\partial^2 u}{\partial \tau^2} = c^2 \frac{\partial^2 u}{\partial x^2} \quad \text{with} \quad c^2 = \frac{1}{\rho \cdot s_{33}} \quad (10)$$

To account for mechanical losses, including material damping, losses in the bonding between electrodes and piezo-material, and losses in the surrounding resin, the effective complex compliance $s_{33}^* = s_{33} \cdot (1 - i\eta)$ was introduced.

The excitation voltage is assumed to consist of superposed DC and AC components, i.e.,

$$V(\tau) = V_0 + V_a e^{i\omega\tau} \quad (11)$$

where V_0 and V_a are the bias and the amplitude voltages respectively.

This model assumes that: (i) the stack can be assimilated to an uniform continuum; (ii) the excitation angular frequency, ω , is much smaller than the ratio between wave speed, c , and the stack length, L ; and (iii) the electric field distribution within the material is relatively uniform, $E_3 = V/t$. The boundary conditions associated with Equation (10) are:

$$u(x_3 = 0, \tau) = 0, \quad A \cdot T_3(x_3 = L, \tau) = F_{ST}(\tau) \quad (12)$$

where $F_{ST}(\tau)$ is the force exerted in the piezo-stack. F_{ST} is made up of two components $F_{ST}(\tau) = F_b + F_a(\tau)$

where: (i) F_b is the bias force given by the internal spring prestress, F_0 , external preload, F_e , and the bias voltage V_0 ; (ii) $F_a(\tau)$ is the oscillatory component that can be related to the velocity of the top of the stack through:

$$F_a(\tau) = -Z_{EXT}(\omega) \cdot \left(\frac{\partial u}{\partial x_3} \right)_{x_3=L, \tau} \quad (13)$$

where $Z_{EXT}(\omega)$ is the external structure impedance.

Denote $\gamma = \omega/c$ and assume a displacement solution of the form:

$$u(x_3, \tau) = (C_1 \sin(\gamma x_3) + C_2 \cos(\gamma x_3))e^{i\omega\tau} - C_3 x_3 \quad (14)$$

The first boundary condition at $x_3=0$ yields $C_2 e^{i\omega\tau} = 0, \forall \tau$. Hence, $C_2 = 0$. At $x_3 = L$,

$$S_3(x_3 = L, \tau) = \left(\frac{\partial u_3}{\partial x_3} \right)_{x_3=L} = \gamma C_1 \cos(\gamma L) e^{i\omega\tau} - C_3 \quad (15)$$

Using Equations (2), (12), (14), (15) yields:

$$C_1 = \frac{d_{33}^* V_a}{t} \left(\gamma \cos(\gamma L) + \frac{s_{33}^*}{A} i\omega Z_{EXT}(\omega) \sin(\gamma L) \right)^{-1},$$

$$C_3 = - \left(\frac{s_{33}^*}{A} F_b + \frac{d_{33}^*}{t} V_0 \right) \quad (16)$$

with $d_{33}^* = d_{33}(1 - i\lambda)$, where λ accounts for the imperfect piezoelectric energy conversion (Holland, 1967). The bias force F_b in Equation (16) is expressed using Equation (8) with $V=V_0$:

$$F_b = F_0 + F_e^{(b)} \cdot \frac{k_{ST}^*}{k_{ST}^* + k_{SP}} - \frac{d_{33}^* \cdot V_0}{t \cdot s_{33}^*} \frac{k_e + k_{SP}}{k_{ST}^* + k_e + k_{SP}}$$

where $F_e^{(b)}$ is the static compressive force applied to the actuator prior to the voltage being applied.

$$u(x_3, t) = \frac{d_{33}^* V_a e^{i\omega\tau}}{t}$$

$$\times \left(1 + \frac{s_{33}^* i\omega Z_{EXT}(\omega)}{A \gamma} \tan(\gamma L) \right)^{-1} \frac{\sin(\gamma x)}{\gamma \cos(\gamma L)}$$

$$+ x_3 \left[\frac{s_{33}^*}{A} \left(F_0 + F_e^{(b)} \frac{k_{ST}^*}{k_{ST}^* + k_{SP}} \right) + \frac{d_{33}^*}{t} V_0 \frac{k_{ST}^*}{k_e + k_{SP} + k_{ST}^*} \right] \quad (17)$$

For the generic external load consisting of a mass-spring-damper system (Figure 1b), we can write:

$$k_d(\omega) = i\omega Z_{EXT}(\omega) = m(\omega_n^2 - \omega^2) + i\omega c_d$$

$$\text{with } \omega_n = \left(\frac{k_e + k_{SP}}{m} \right)^{1/2} \quad (18)$$

Hence, the actuator displacement, $u_{ST} = u(x_3=L, \tau)$, becomes:

$$u_{ST}(\tau) = \frac{d_{33}^* V_a \tan(\gamma L) e^{i\omega\tau}}{t\gamma(1 + (s_{33}^*/A)(k_d(\omega)/\gamma) \tan(\gamma L))} + \frac{F_e^{(b)}}{k_{ST}^* + k_{SP}}$$

$$+ \frac{L}{t} d_{33}^* V_0 \frac{k_{ST}^*}{k_{ST}^* + k_{SP} + k_e} \quad (19)$$

Using Equation (19) in Equation (2), and recalling $F_{ST}(\tau) = A \cdot T_3(x_3 = L, \tau)$, the force exerted in the piezo-stack is:

$$F_{ST}(\tau) = -F_{\text{block}} \frac{V_a}{V_0} e^{i\omega\tau} \left(1 + \frac{s_{33}^* k_d(\omega)}{A \gamma} \tan(\gamma L) \right)^{-1}$$

$$+ F_0 + F_e^{(b)} \frac{k_{ST}^*}{k_{ST}^* + k_{SP}}$$

$$+ F_{\text{block}} \left(\frac{k_e + k_{SP}}{k_e + k_{SP} + k_{ST}^*} + \frac{V_a}{V_0} e^{i\omega\tau} \right) \quad (20)$$

where F_{block} is the static blocked force corresponding to the bias voltage, V_0 , i.e.,

$$F_{\text{block}} = - \frac{d_{33}^* A}{s_{33}^* t} V_0 \quad (21)$$

The external force can be expressed as:

$$F_e(\tau) = F_{ST}(\tau) - k_{SP} u_{ST}(\tau) - F_0 \quad (22)$$

To model the electric current, the second part of Equation (2) is written as:

$$D_3 = d_{33}^* \frac{F_{ST}(\tau)}{A} + \frac{\epsilon_{33}^*}{t} (V_0 + V_a e^{i\omega\tau}) \quad (23)$$

where the electric field was replaced by $E = V/t$, and electric losses were modeled as $\epsilon_{33}^* = \epsilon_{33}(1 - i\delta)$. The electric displacement \mathbf{D} is related to the free charge distribution, ρ_f , by the equation $\text{div } \mathbf{D} = \rho_f$ (Maxwell, 1891). For one-dimensional geometry, this equation reduces to $Q = D_3 A$, where Q is the free charge accumulated on the electrodes. The instantaneous

current is the partial derivative of the free charge with respect to time:

$$i_{ST}(\tau) = \frac{dQ}{d\tau} = \frac{L}{t} i\omega V_a e^{i\omega\tau} \times \left[d_{33}^* F_{\text{block}} \left(\left(1 + \frac{s_{33}^* k_d(\omega)}{A \gamma} \tan(\gamma L) \right)^{-1} - 1 \right) + \frac{\epsilon_{33}^* A}{t} \right] \quad (24)$$

The actuator electrical impedance is given by:

$$Z_{ST}(\omega) = \frac{V_a e^{i\omega\tau}}{i_{ST}(\tau)} = \frac{1}{i\omega L} \times \left[d_{33}^* F_{\text{block}} \left(\left(1 + \frac{s_{33}^* k_d(\omega)}{A \gamma} \tan(\gamma L) \right)^{-1} - 1 \right) + \frac{\epsilon_{33}^* A}{t} \right]^{-1} \quad (25)$$

The instantaneous power is given by $p(\tau) = i_{ST}(\tau) \cdot v(\tau)$. The average active power per cycle can then be calculated as:

$$P_a = f \cdot \int_{\text{cycle}} p(\tau) d\tau = f \cdot \int_0^{2\pi/\omega} v(\tau) \cdot i_{ST}(\tau) d\tau \quad (26)$$

where $v(\tau)$ and $i_{ST}(\tau)$ are given by Equations (11) and (24), respectively.

EXPERIMENTAL CHARACTERIZATION OF PIEZOELECTRIC STACK ACTUATORS

The purpose of the experiments was to evaluate the blocked force, the characteristic loops, and the mechanical and electrical envelopes for a piezoelectric stack actuator PAHL 120/20, in quasi-static and dynamic regimes. The characteristic loops considered here are force–displacement, current–voltage, and voltage–displacement curves. The mechanical envelope for a given frequency correlates the extreme values of voltage, displacement, and force. Likewise, the electrical envelopes correlate force and voltage with the peak or the active power, respectively.

Experimental Setup

The signal generated by a Hewlett Packard HP 3312A function generator was amplified by a high-voltage 2-channel TREK 750/50 amplifier, and sent to the PAHL 120/20 actuator (Figure 2). To increase the dynamic range, the two channels of the TREK 750/50 amplifier were merged. The amplified signal was tapped to the HP5460B digital oscilloscope. A parallel

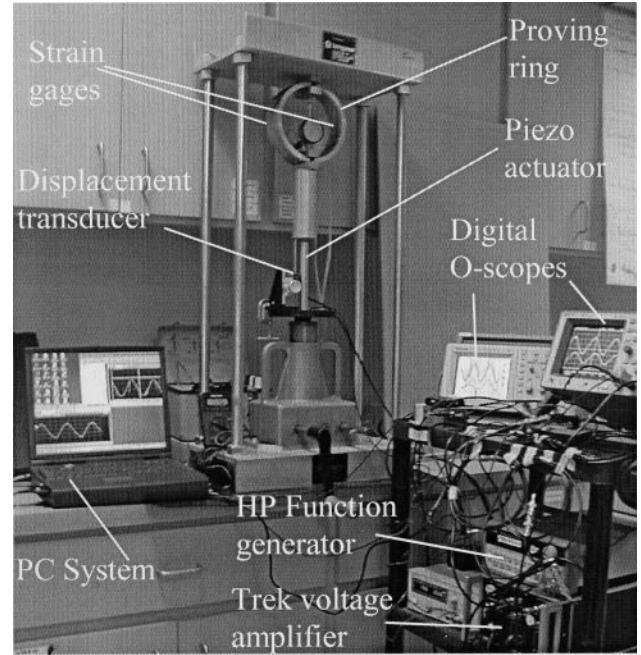


Figure 2. Experimental setup for dynamic testing of PAHL 120/20.

circuit consisting of a 1 k Ω resistor and a normally open switch was used for discharging the stack. The current going through the actuator was measured using the voltage drop across a calibrated 1 Ω resistor placed in series with the actuator. This signal was passed through a low-pass filter and displayed on the second channel of the HP5460B. The displacement of the actuator was measured with a Philtec D100 optical displacement transducer and sent to a Tektronix TDS210 digital oscilloscope (Figure 3a). The external load was applied using a LongYear compression frame and a proving ring. The proving ring was equipped with a dial gauge calibrated to measure force (accuracy ± 7.2 N) (Figure 3b) and four strain gages in full bridge configuration. The strain gage signal was passed through a low-pass filter and displayed on the second channel of the TDS210. The 4 waveforms captured on the digital oscilloscopes were downloaded into a PC.

The measurements were taken in static and dynamic regimes. The maximum frequency attained during the dynamic regime was $f_C \approx 5$ Hz. For a capacitive load, the maximum achievable frequency is limited by the maximum electric current capability of the power amplifier (Figure 4). Given the 0.1 A maximum current of the TREK 750/50 amplifier, a voltage duty-cycle of 0–150 V, and the PAHL 120/20 piezoelectric actuator capacitance of 42 μ F, yields a predicted maximum frequency of 7.1 Hz. Experimental results showed current saturation of the power supply to appear at as low as 5 Hz, and thus the highest testing frequency used in our experiment was $f_C = 5$ Hz.

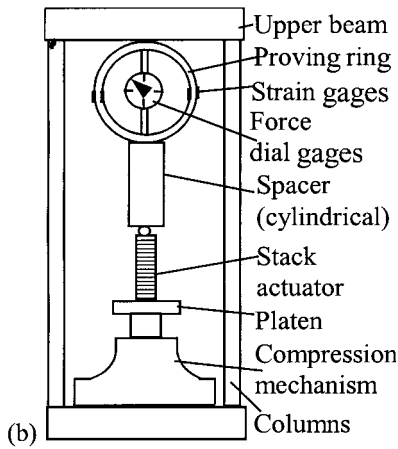
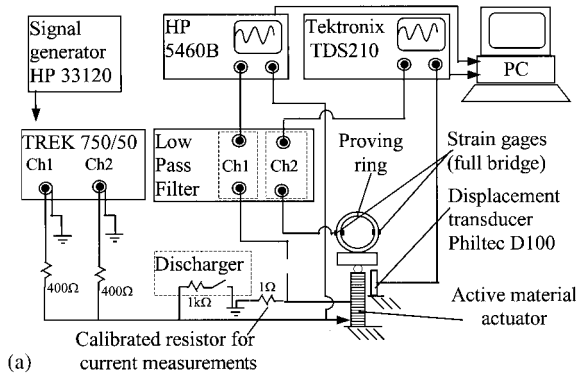


Figure 3. (a) Schematic for the experimental setup for the piezo-electric PAHL 120/20 actuator; (b) compression frame.

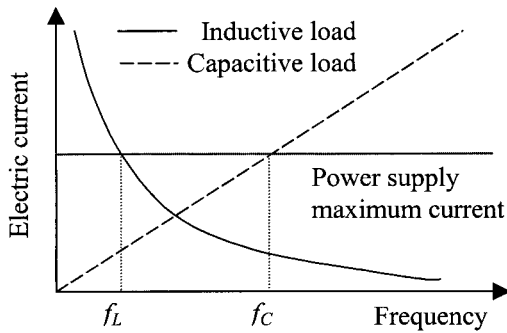


Figure 4. Power supply frequency restrictions for the operation of inductive and capacitive loads.

Measurements Procedures and Results

MEASUREMENTS OF THE BLOCKED FORCE

The blocked force is defined as the force developing in the actuator when pushing against a body of infinite stiffness, such that no external displacement is possible and all the induced strain is consumed internally. Since the compression frame does not have an infinite stiffness, special methods had to be devised to create the condition of zero external displacement.

Static Method 1 Apply a given voltage, thus expanding the stack, and then compress the actuator until the net displacement is brought back to zero. The following steps were applied:

- Discharge the unloaded actuator, zero the signal generator and switch on the amplifier;
- Adjust the platen supporting the actuator (Figure 3b) until its tip positively contacts the proving ring;
- Mark the initial position of the displacement signal with the oscilloscope cursor;
- Increase the voltage up to the first voltage level: the stack expands and the proving ring compresses;
- Adjust the platen to compress the assembly until the displacement signal returns to the initial position marked by the cursor. When this step is completed the stack has recovered its initial length, and the force recorded by the proving ring is the blocked force for the given voltage.
- Repeat from (d) for the other voltage levels.

Static Method 2 Compress the stack to a given force, and then adjust the voltage until the initial length of the stack is recovered. Record the final voltage and force values. This method is done in the following steps:

- Discharge the unloaded stack, zero the signal generator and switch on the amplifier;
- Mark the initial position of the displacement signal using the oscilloscope cursor;
- Introduce the first prestress level by compressing the actuator with the platen against the proving ring;
- Increase the voltage until the displacement signal on the oscilloscope returns to the initial position and read the final voltage and the corresponding blocked force.

Dynamic Method The following steps were used:

- Discharge the unloaded stack and bring the stack in contact with the proving ring;
- Set the first voltage duty cycle on the signal generator and turn on the amplifier – the voltage, displacement, and force will harmonically cycle between zero and the maximum value; place the oscilloscope cursor on the minimum value of the displacement waveform;
- Compress the assembly by adjusting the platen until the maximum value of the displacement waveform coincides with the oscilloscope cursor;
- Record the blocked force value as the maximum of the force waveform;
- Repeat for other voltage duty cycles.

The results of blocked force measurements for static and dynamic excitation are shown in Figure 5. Superposed on Figure 5 is also the theoretical line predicted by Equation (21). As seen from Figure 5, the

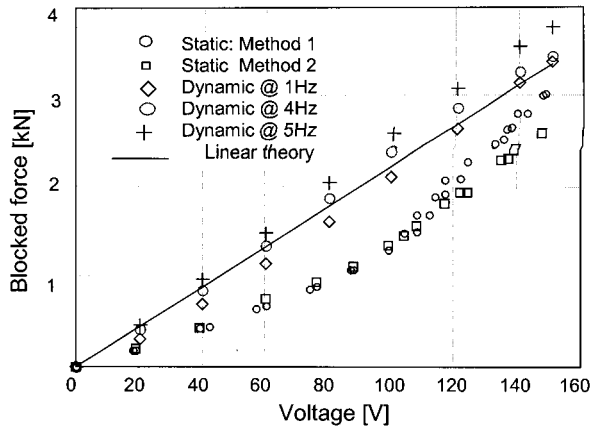


Figure 5. Blocked force variation with voltage: theory and experiment.

linear theory over-predicts the quasi-static blocked force measurements, but seems to be a good approximation to the dynamic blocked force measurements.

Regarding the static data, the two testing methods give similar results for voltages up to 70% of the maximum value. At higher voltages, the results of the two methods start to diverge, with 14% maximum difference being observed at 150 V.

STATIC AND DYNAMIC ACTUATOR CHARACTERIZATION

To completely describe the piezoelectric actuator behavior under quasi-static and dynamic conditions, the actuator displacement under combined electro-mechanical load (force and voltage) had to be recorded. Due to the spring-like character of the external load, distinction had to be made between the measurement procedures for the points situated above and respectively below the external stiffness line of Figure 6.

For points situated above and on the external stiffness line, the following steps were taken:

- Discharge the stack and bring the push-rod in contact with the proving ring;
- Superpose the first oscilloscope cursor on the displacement signal and record the initial position v_1 ;
- Compress the whole assembly up to the first prestress level;
- Apply the first voltage level, V : the actuator expands and the proving ring further compresses;
- Move the second oscilloscope cursor until it superposes on the displacement signal on the oscilloscope display, and record v_2 . The displacement of the actuator is given by $v_2 - v_1$;
- Read the compressive force F ;
- Repeat from step (d) for other voltage levels, up to the maximum voltage;

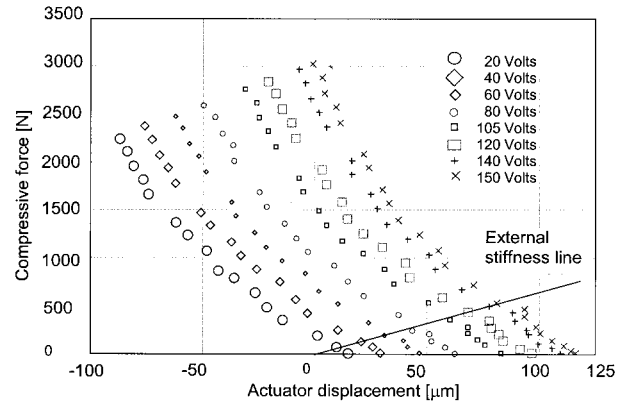


Figure 6. Force–displacement–voltage correlation.

- Repeat from step (c) for the other prestress levels.

Data points evaluated using this procedure lie on curves parallel to the external stiffness curve, above it. This procedure cannot be used for the determination of the points situated below the external stiffness line, because this would require placing the stack in tension.

For points below the external stiffness line, the following procedure was used:

- Discharge the stack;
- Apply an initial voltage to the unloaded actuator;
- Bring the top of the actuator in contact with the bottom of proving ring;
- Apply a higher voltage, V , and record the force, F , and the displacement, u ;
- Repeat from step (d) for the other voltage levels up to the maximum voltage;
- Repeat from step (a) with higher initial voltages.

The data points will also lie on curves parallel to the external stiffness curve, but situated below it (Figure 6).

The procedure for dynamic measurements resembles the procedure used for static measurements, with modifications to account for the dynamic effects. The excitation voltage was of the form given in Equation (11), with $V_a = V_0$.

For the points situated above and on the external stiffness curve, the following procedure was used for each tested frequency:

- Discharge the stack and set the desired prestress level by compressing the actuator with the platen against the proving ring;
- Set the voltage duty-cycle on the function generator and turn on the amplifier;
- Download the waveforms into the PC;
- Repeat from step (b) for the next voltage duty-cycle, up to the maximum allowable voltage;
- Repeat from step (a) for the next prestress level, up to the prestress corresponding to the blocked force for maximum allowable voltage.

Dynamic data was complemented with no-load measurements of the piezoelectric actuator for each frequency.

DATA PROCESSING AND COMPARISON WITH THEORETICAL PREDICTIONS

Static Results

Figure 7 indicates that the piezoelectric linear static model shows good correlation with experimental results for zero load. However, the static model is a poor predictor for the static behavior of the piezostack under high force condition, which shows significant non-linearity. The experimentally observed deviations from the linear model were addressed through coefficient tuning, using a bivariate cubic regression of the actuator displacement (Figure 8):

$$u = C_0 F_e^3 + C_1 F_e^2 V + C_2 F_e V^2 + C_3 V^3 + C_4 F_e^2 + C_5 F_e V + C_6 V^2 + C_7 F_e + C_8 V \quad (27)$$

Besides the intrinsic behavior of the piezoelectric material under electro-mechanical loading, the overall

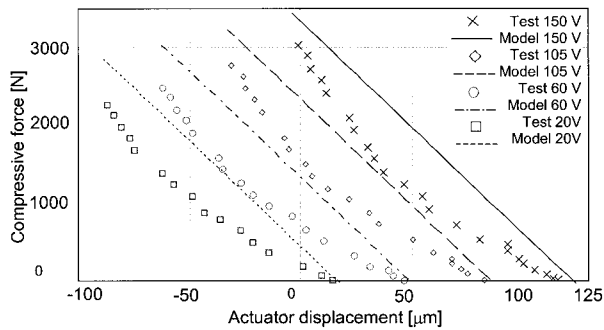


Figure 7. Comparison of the PiezoSystems Jena actuator static linear model prediction with experimental data.

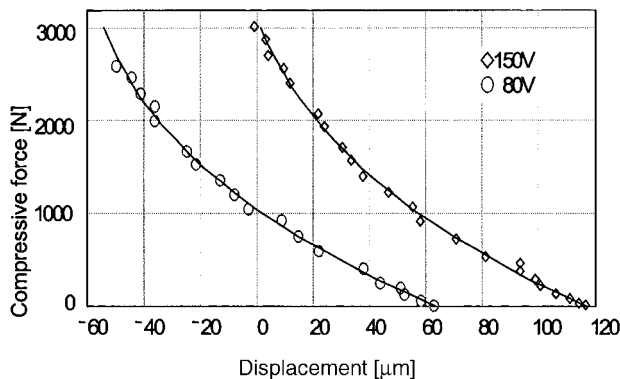


Figure 8. Curve-fitting of experimental data using a bivariate regression.

actuator displacement also contains the influence of the prestress spring, electrodes, and resin. The nonuniform electric-field distribution inside the active material layer also adds nonlinearity to the actuator behavior. Nevertheless, an approximate description of the overall actuator characteristics under electro-mechanical loading can be obtained, if we neglect the effect of electrodes, resin and electric field nonuniformity. The force in the active material stack, F_{ST} , is simply the sum of the measured force and the force exerted by the prestress spring, k_{SP} , i.e.,

$$F_{ST} = F_e + F_0 - k_{SP} \cdot u \quad (28)$$

where F_e is the external force, and u is the actuator displacement. Substitution of Equation (28) into the regression Equation (27) provides the full description of the overall actuator behavior, in terms of the force in the active material, F_{ST} , voltage and actuator displacement. Thus, a numeric solution of the form $u = u(F_{ST}, V)$ could be determined.

ACTUATOR STATIC STIFFNESS

For nonlinear behavior, the actuator stiffness can be defined as the local derivative of the force–displacement curve (tangent stiffness) or as the ratio of the local force and displacement values (secant stiffness). To calculate the tangent stiffness, we used the inverse of the tangent compliance, i.e. $k = (\partial u / \partial F_e)^{-1}$. The results presented in Figure 9 indicate that the tangent stiffness of the piezoelectric actuator increased significantly with the compressive mechanical load. The variation of the actuator stiffness with voltage is, however, almost negligible.

COMPLIANCE AND PIEZOELECTRIC COEFFICIENTS

If we assume that the piezoelectric material behavior is sufficiently well described by the law $S_{33} = s_{33}(V, F) \cdot F + d_{33}(V, F) \cdot V$, the displacement derivatives with respect to force and voltage can be written as:

$$\begin{aligned} \frac{A}{L_i^0} \left(\frac{\partial u}{\partial F_{ST}} \right) &= s_{33} + F \frac{\partial s_{33}}{\partial F_{ST}} + \frac{A}{t} V \frac{\partial d_{33}}{\partial F_{ST}}, \\ \frac{t}{L_i^0} \left(\frac{\partial u}{\partial V} \right) &= \frac{t}{A} F_{ST} \frac{\partial s_{33}}{\partial V} + V \frac{\partial d_{33}}{\partial V} + d_{33} \end{aligned} \quad (29)$$

By neglecting the cross-coupling terms, (ANSI/IEEE Std.176, 1987; Mitrovic et al., 1999) we obtain a first-order approximation of the compliance and

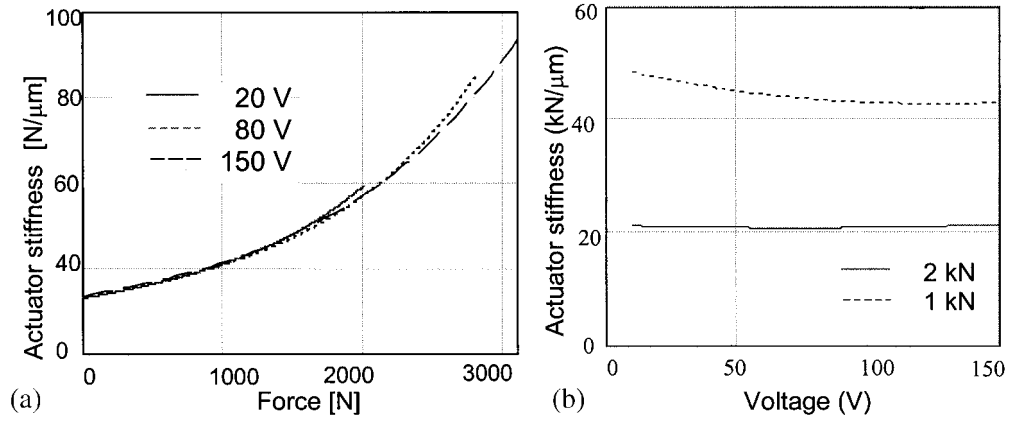


Figure 9. Actuator stiffness: (a) variation with external force; (b) variation with voltage.

piezoelectric coefficients for the active material of the tested actuator:

$$s_{33} \approx \frac{A}{L_i^0} \left(\frac{\partial u}{\partial F_{ST}} \right); \quad d_{33} \approx \frac{t}{L_i^0} \left(\frac{\partial u}{\partial V} \right) \quad (30)$$

The resulting s_{33} and d_{33} curves are presented in Figure 10. The compliance coefficient, s_{33} , is seen to decrease with increasing stress (Figure 10a) and not to vary significantly with the applied electric field. The piezoelectric coefficient d_{33} displays a maximum value at approximately half the maximum electric field. Its dependence on stress is not negligible (Figure 10b).

Dynamic Results

DATA PROCESSING

For each frequency–prestress–voltage case, four waveforms (displacement, force, current, voltage) were recorded and further processed in several stages using Matlab™ software (Figure 11). The first stage of data processing consisted of:

- (a) Adjust the current and force related signals to account for the phase and amplitude change introduced by the analog low-pass filter, using the filter calibration;
- (b) Filter out the spikes from the electric current, force and displacement related waveforms using a cascaded algorithm for outliers elimination;
- (c) Apply a high-order Butterworth digital filter to all four waveforms (Figure 12);
- (d) Use the calibration data for the proving ring, strain gages full-bridge, and the 1Ω resistor to convert electrical waveforms into force, electric current, and displacement waveforms.

The next stage of data processing consisted of building the characteristics loops of synchronized waveforms, paired as follows: displacement versus force, current versus voltage, and displacement versus voltage (Figure 13d–f). These characteristic loops for

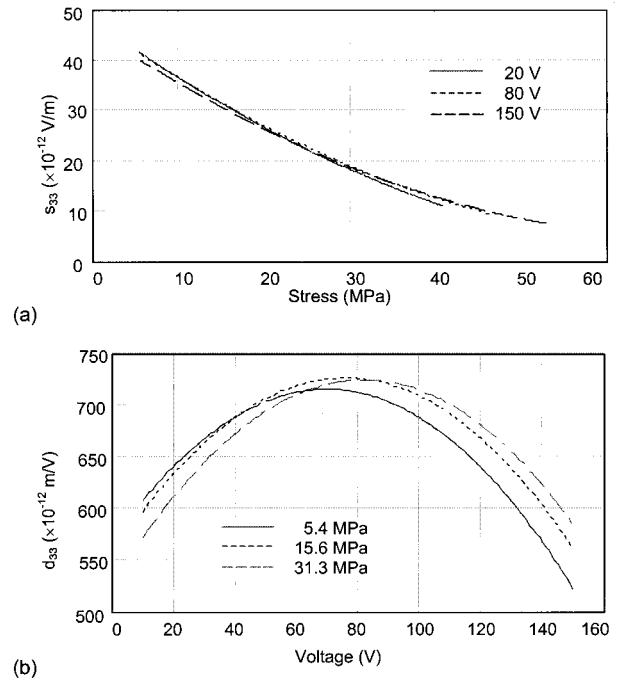


Figure 10. Effective piezoelectric material coefficients evaluated from the derivatives of the displacement with respect to force and voltage: (a) compliance, s_{33} ; (b) piezoelectric coefficient, d_{33} .

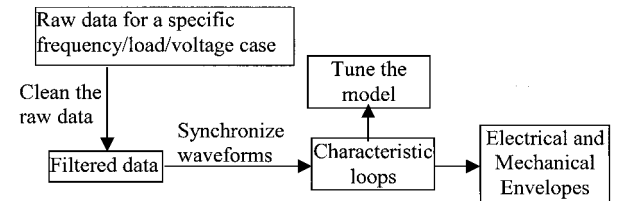


Figure 11. Data processing logic flow.

each frequency–prestress–voltage range were used for tuning the dynamic model of the actuator.

Finally, the mechanical and electrical envelopes were synthesized using the extreme values of the characteristic loops (Figures 16–18). These envelopes give a general view of actuator capabilities and point to its usefulness for specific applications.

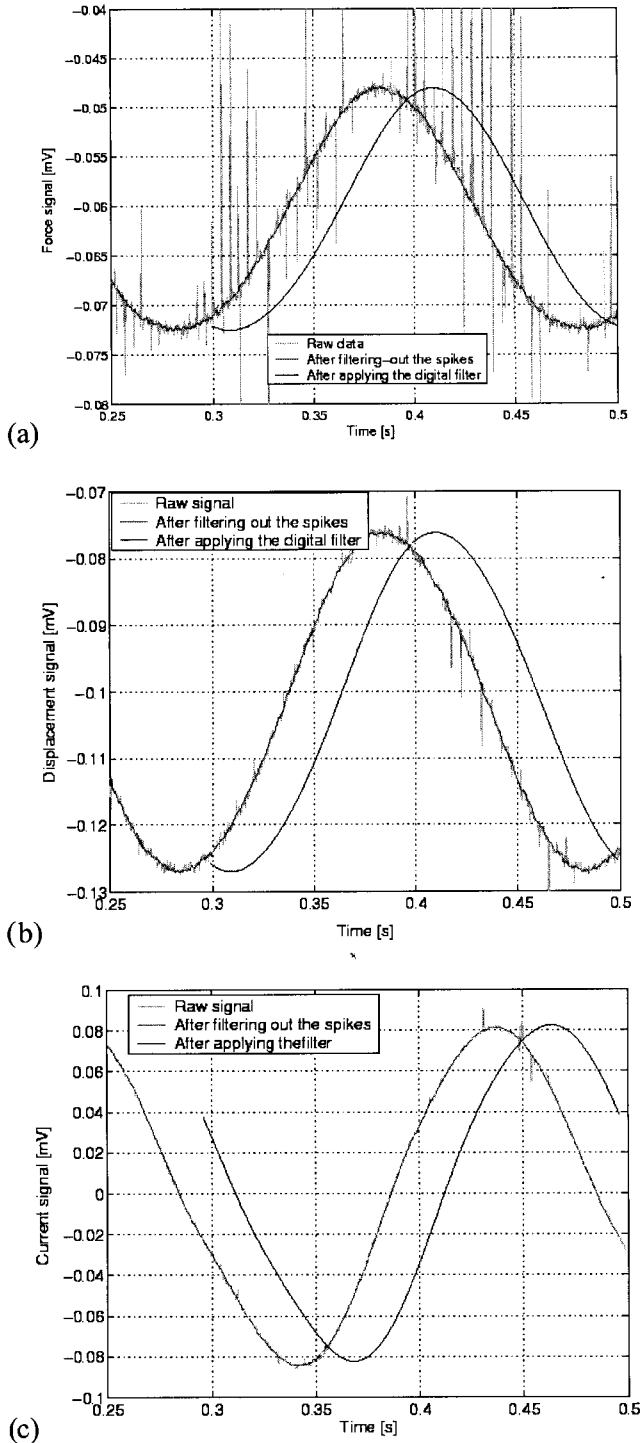


Figure 12. Signal processing steps simultaneously shown on the same chart (5 Hz, 1150 N prestress, 0–100 V): (a) force; (b) displacement; (c) electric current.

TUNING AND IMPROVEMENT OF THE DYNAMIC MODEL

The dynamic model parameters and their observed correlation with the actuator behavior are listed in Table 2. The values of these parameters were determined by tuning the theoretical model prediction to the

experimental data. During this process, special attention was given to the parameters ε_{33} and δ , which represent the dielectric permittivity and dielectric loss, respectively. Unlike the other model parameters that could be assumed constant throughout a loading–unloading cycle, ε_{33} and δ had to be allowed to vary during the cycle. While the dynamic model predicted sinusoidal electric current waveforms, the experimental results showed significant deviations from the harmonic waveform on the electro-mechanical unloading path (Figure 13c). During unloading, the measured current lags behind the linear-model prediction, and the instantaneous minimum current is smaller in absolute value than the maximum current. In order to account for these phenomena, the following nonlinear laws of ε_{33} and δ variation inside the cycle were used:

$$\varepsilon_{33} = \varepsilon_0[1 - 0.5(k_\varepsilon - 1)f_c(t)(H(t_{\text{end}}) - H(t_{\text{start}}))] \quad (31a)$$

$$\delta = \delta_0[1 + 0.5(k_\delta - 1)f_c(t)(H(t_{\text{end}}) - H(t_{\text{start}}))] \quad (31b)$$

where ε_0 and δ_0 are the values during the loading half-cycle, and k_δ and k_ε are numerical values that account for the phase shift and amplitude reduction of the electric current respectively. $H(t)$ is the Heaviside function with t_{start} and t_{end} being the start and the end of the electro-mechanical unloading part of the cycle. The function $0.5 f_c(t)(H(t_{\text{end}}) - H(t_{\text{start}}))$ is a Hanning window, which ensures smooth transition between the loading and unloading portions of the cycle (Figure 14). The improved model correlates better with the observed actuator behavior, as shown in Figure 15.

Thus, for each combination of frequency, voltage, and prestress, a set of 8 effective parameters were determined: d_{33} , λ , s_{33} , η , ε_0 , δ_0 , k_δ , k_ε (Table 3).

DISCUSSION

The blocked force for a given voltage is an important parameter in describing a piezoelectric actuator, because it helps to establish an estimate of the available actuating energy under static loading (Figure 16). The two experimental methods devised for blocked force estimation showed consistency for voltages up to 70% of the maximum voltage. Above this value, the two methods started to depart from each other, with as much as 14% difference being observed at 150 V. These results indicate that the hypothesis of linear superposition holds only up to 70% of the operational range. Above 70%, ferroelastic and ferroelectric switching time-history effects seems to become important, since the same inputs applied in a different order lead to different electro-mechanical equilibrium states. The

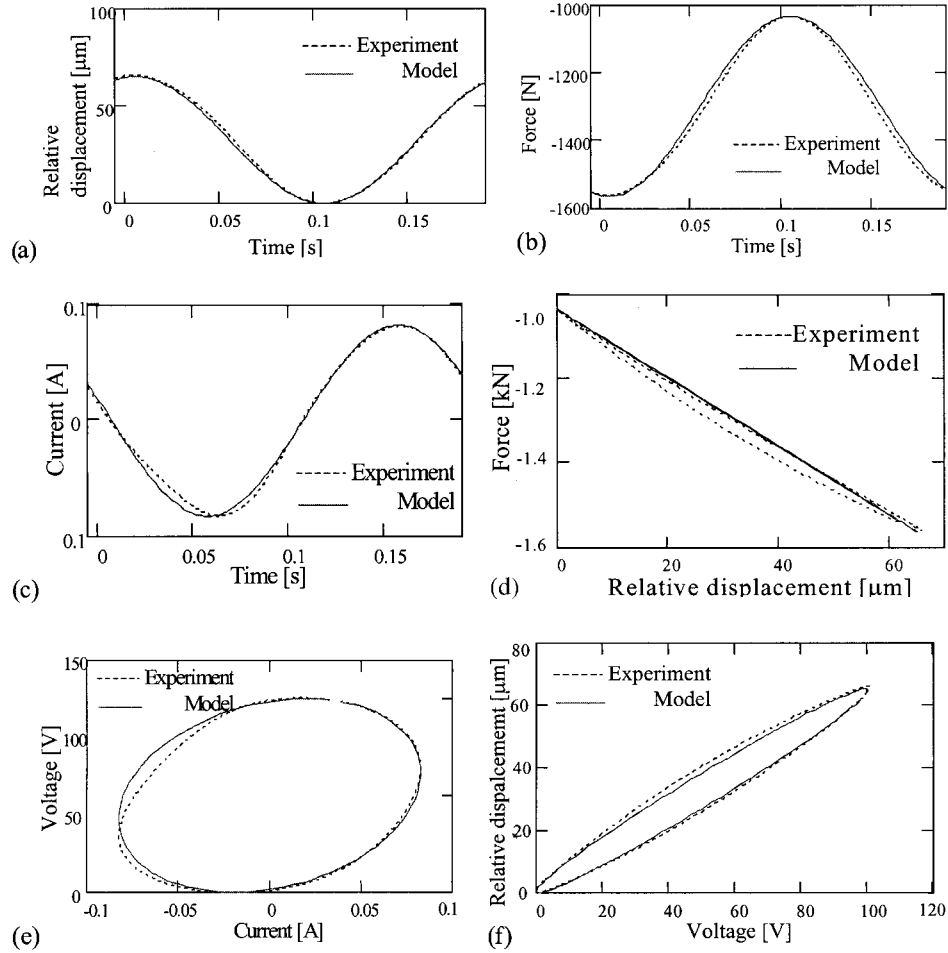


Figure 13. Comparison of experimental data with the model prediction for 5Hz, 1150 prestress and 0–100V: (a) displacement waveform; (b) force waveform; (c) electric current waveform; (d) displacement–force loop; (e) electric current–voltage loop; (f) voltage–displacement loop.

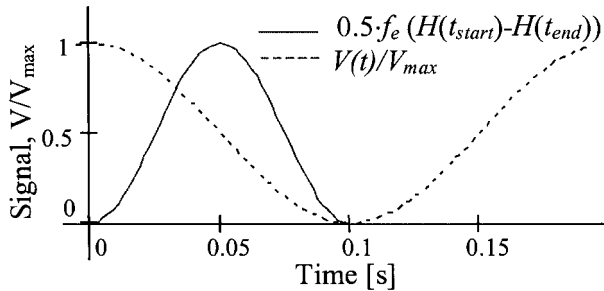


Figure 14. Hanning window acting on the unloading part of the cycle.

explanation for this behavior resides in the different net number of ferroelastic domain switching that occurs when the order of loading is changed. For dynamic loading, these ferroelectric–elastic switching effects seem to reach a state of dynamic equilibrium, which yields an almost linear dependence between voltage and blocked force. In addition, trends of increased blocked force with frequency were also observed, indicating that the time-history effects are not negligible even for the limited frequency range tested.

For dynamic application, effective values of model parameters (Table 3) were obtained in a cycle-average sense. Since most of the parameters display a consistent pattern of variation when frequency, voltage range, and prestress level are varied, interpolation of the data in Table 3 between the tested cases seems appropriate for the tested actuator.

Data presented in Table 3 suggests that the cycle-equivalent value of the d_{33} coefficient increases with voltage. This can be explained through the increased number of domain ferroelastic switching when the voltage is cycled to a higher value. The cycle-equivalent values of d_{33} are consistent with the corresponding static data (Figure 10b), when the bias voltage is varied.

The electrical envelopes for the maximum peak power show a consistent dependence on frequency, force, and voltage cycle (Figure 17), qualifying the peak power as a useful indicator when evaluating a piezoelectric actuator for a specific application. Hence, besides the expected proportionality with the applied voltage and frequency, the peak power is seen also to increase with force. This increase (up to 10%), may be due to an increased dielectric permittivity along a direction that is no longer

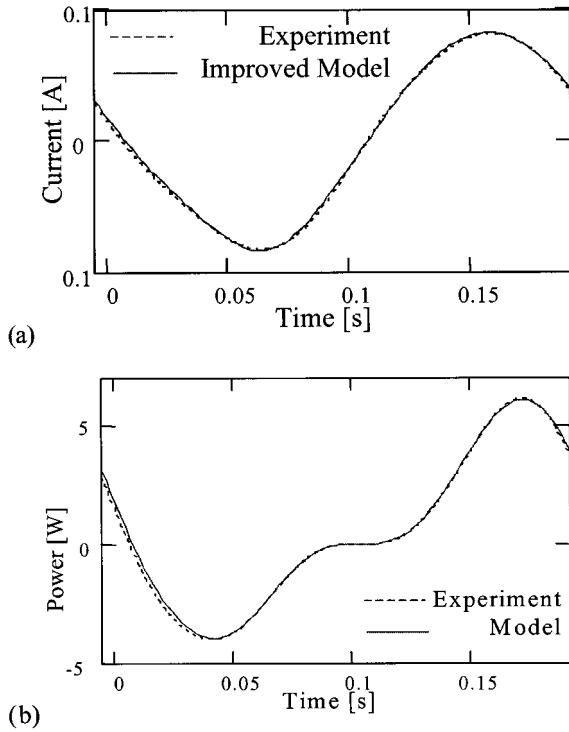


Figure 15. Improved model predictions for: (a) electric current; (b) instantaneous power.

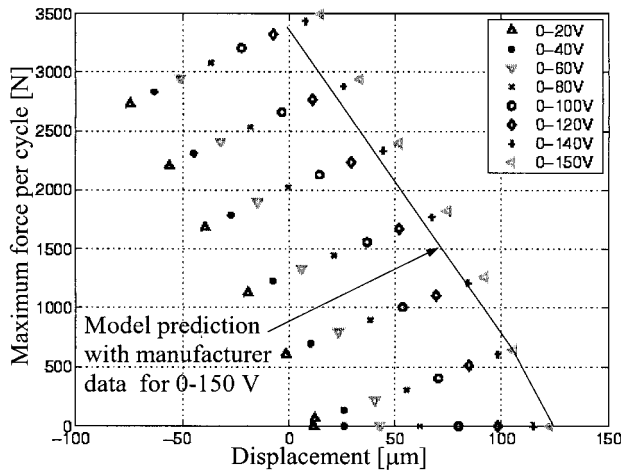


Figure 16. Mechanical envelope for the piezoelectric actuator PiezoSystems Jena PAHL 120/20 under dynamic testing at 5 Hz.

aligned with the dipole axis of the PZT crystal, due to inherent crystal anisotropy (Du et al., 1997; Uchino, 2000). As the stress increases, more ferroelastic switches occurs, leading to more domains having their electric dipoles misaligned from the x_3 axis, resulting in an increased permittivity at the polycrystallite level. The behavior of the cycle-equivalent electrical permittivity, ϵ_{33} , correlates well with this explanation.

The average active power per cycle consumed by the actuator (Figure 18) appears to show a trend towards increasing with the voltage and decreasing with

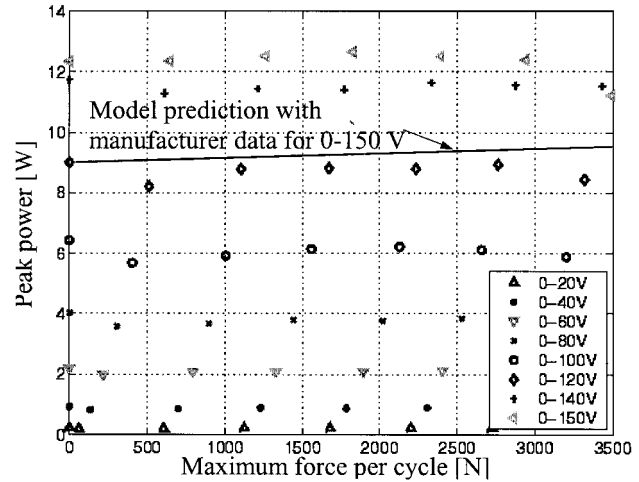


Figure 17. Electrical envelope for the PiezoSystems Jena PAHL 120/20: peak power at 5 Hz.

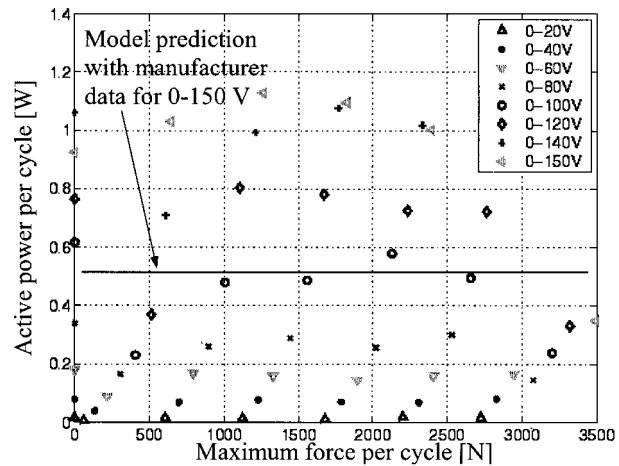


Figure 18. Electrical envelope for the PiezoSystems Jena PAHL 120/20: active power at 5 Hz.

Table 2. Correlation between tuning coefficients and experimental curves.

Material Parameter	Influence on the Characteristic Curves
d_{33}	Proportional to the amplitude of the displacement waveform and the secant slope of the force–displacement characteristic loop. Influences amplitudes of the force and displacement waveforms
s_{33}	The ratio of the stack stiffness k_{ST} to the external dynamic stiffness k_d influences the slope of the force–displacement loop.
ϵ_{33}	Related to the electric current amplitude on the loading path.
λ	Proportional with the hysteresis in the displacement–voltage characteristic loop.
η	No significant influence.
δ	Global tilt of the current–voltage characteristic loop.

Table 3. Piezoelectric model parameters – variation with frequency, voltage and prestress level.

Voltage Range	λ	$d_0 \times 10^{-12}$	$\epsilon_0 \times 10^{-8}$	$s_{33} \times 10^{-12}$	κ_{33}	δ_0	k_δ	$\delta_0 \cdot k_\delta$	k_ϵ
1 Hz, External load not coupled									
0–60 V	0.03	650	7.1	20.8*	0.29*	0.13	2.0	0.26	1.00
0–100V	0.08	730	7.7	20.8*	0.33*	0.10	4.5	0.45	1.06
0–150V	0.07	750	7.8	20.8*	0.35*	0.05	12.0	0.60	1.10
1 Hz, \approx 1100N Prestress									
0–60 V	0.08	620	7.2	15	0.36	0.13	1.5	0.20	1.00
0–100 V	0.03	665	7.6	15	0.39	0.15	2.6	0.39	1.01
0–150 V	0.04	710	8.0	17	0.37	0.05	12.0	0.60	1.09
1 Hz, \approx 2840 Prestress									
0–60 V	0.10	600	7.5	13	0.37	0.14	1.6	0.22	1.00
0–100 V	0.07	650	8.1	13	0.40	0.11	3.3	0.36	1.05
0–150 V	0.04	690	8.2	13	0.45	0.03	15.0	0.45	1.05
2 Hz, External load not coupled									
0–60 V	0.30	630	7.3	20.8*	0.26*	0.10	1.8	0.18	1.07
0–100 V	0.10	710	7.7	20.8*	0.32*	0.10	3.3	0.33	1.04
0–150 V	0.07	720	7.6	20.8*	0.33*	0.05	12.0	0.60	1.10
2 Hz, \approx 1100N Prestress									
0–60 V	0.10	610	7.1	15	0.35	0.12	1.5	0.18	1.00
0–100 V	0.03	665	7.6	15	0.39	0.10	3.0	0.3	1.01
0–150 V	0.03	710	7.8	15	0.43	0.01	40.0	0.4	1.06
2 Hz, \approx 2840 Prestress									
0–60 V	0.03	590	7.5	13	0.36	0.12	1.4	0.17	1.00
0–100 V	0.03	630	7.9	13	0.38	0.12	3.3	0.4	1.07
0–150 V	0.08	690	8.1	13	0.45	0.03	15.0	0.45	1.07
4 Hz, External load not coupled									
0–60 V	0.03	570	6.8	20.8*	0.23*	0.27	1.5	0.41	1.03
0–100 V	0.08	630	7.4	20.8*	0.26*	0.14	3.5	0.49	1.06
0–150 V	0.07	650	7.5	20.8*	0.27*	0.05	12.0	0.60	1.13
4 Hz, \approx 1100N Prestress									
0–60 V	0.01	580	6.9	15	0.33	0.15	1.8	0.27	1.02
0–100 V	0.03	660	7.4	15	0.39	0.15	2.8	0.42	1.06
0–150 V	0.05	680	7.5	15	0.41	0.05	12.0	0.6	1.07
4 Hz, \approx 2840 Prestress									
0–60 V	0.03	550	7.2	13	0.27	0.10	2.0	0.20	1.01
0–100 V	0.02	610	7.6	13	0.38	0.12	3.3	0.40	1.06
0–150 V	0.03	660	7.8	13	0.42	0.06	8.0	0.48	1.08
5 Hz, External load not coupled									
0–60 V	0.12	620	6.6	22*	0.27*	0.28	1.5	0.42	1.03
0–100 V	0.17	700	7.0	22*	0.32*	0.30	2.0	0.60	1.10
0–150 V	0.12	720	6.8	22*	0.35*	0.12	5.5	0.66	1.12
5 Hz, \approx 1100N Prestress									
0–60 V	0.12	600	6.9	15	0.35	0.22	1.8	0.40	1.05
0–100 V	0.16	680	7.3	17	0.37	0.25	2.0	0.50	1.08
0–150 V	0.20	690	7.2	17	0.39	0.18	3.7	0.67	1.14
5 Hz, \approx 2840 Prestress									
0–60 V	0.12	570	7.0	16	0.29	0.27	1.6	0.43	1.03
0–100 V	0.17	610	7.6	13	0.38	0.12	3.2	0.38	1.05
0–150 V	0.17	660	7.3	13	0.46	0.02	25	0.5	1.09

prestress level. The increase with voltage is more pronounced than the theory predicts with a constant dielectric loss coefficient, δ . These characteristics could be explained through domain switching: for a given voltage cycle, increasing the prestress is equivalent to

impeding more domains to perform ferroelastic switching, while with a given prestress level, an increased voltage cycle will help more domains to perform 90° switching. Since ferroelastic switching is associated with energy loss, as shown by Kessler and Balke (2001), the

implications to the active power consumption are immediate. These observations correlate with the model coefficients mostly through the variation of the $\delta_0 \cdot k_\delta$ product (Table 3), that represents the peak dielectric loss on the unloading cycle. This quantity represents a better modeling parameter than k_δ , since it captures both the above mentioned measured trends seen in the active power envelopes, and its variation is contained within a narrower range. For example, for the 0–150 V duty cycle, the numerical value of k_δ is found to vary between 6 and 35, depending on the frequency and prestress level, but the variation of the $\delta_0 \cdot k_\delta$ product lies only in the range 0.4–0.6.

CONCLUSIONS

The present work has presented an engineering approach to multidisciplinary characterization of a piezoelectric actuator, using modeling and electro-mechanical measurements.

The thorough characterization of a commercially available piezoelectric actuator (PiezoSystems Jena PAHL 120/20) yielded correlations between output force, displacement, electrical current, and voltage over a wide range of voltages, prestress levels, and frequencies. For high static electro-mechanical loading, it was noticed from the blocked force measurements that the electro-mechanical equilibrium depends on the order of load application, and thus, the loads superposition principle is valid only up to 70% of the maximum voltage. The microstructural ferroelastic effects leading to this behavior also induce a strong nonlinearity in the static mechanical envelope. However, for dynamic loading, this nonlinearity appears to be negligible.

The quasi-linear dynamic model employed in this analysis permitted the evaluation of cycle-averaged parameters influencing the active material behavior, giving a quantitative insight into optimization opportunities arising from varying the prestress and frequency. Comparison of experimental data and model predictions allowed model improvement. The consideration of higher dielectric losses on the unloading path is an important novel feature of the present work. A good metric for these losses was found to be the peak dielectric loss on the unloading path. This parameter was found to increase with voltage cycle and decrease with the level of applied prestress, correlating well with the active power required by the piezoelectric actuator. The microstructure theory of polarization domain switching correlates qualitatively with the observed behavior of the piezoelectric stack.

The measurements of the peak and active power consumed by actuator yielded important characterization charts (electrical envelopes), showing consistent dependence of these quantities on prestress level and voltage duty-cycle. Along with the mechanical envelopes,

they provide a complete data set for the design of actuating systems incorporating piezoelectric actuators.

Although the numerical values and the actuator behavior trends noticed during this study are particular to the actuator under consideration and its piezoelectric material, the characterization approach can be extended to analysis of other actuators of this type.

NOMENCLATURE

- A = cross-sectional area of the stack
- L = length of the stack
- t = active layer thickness
- S_3 = contracted notation for the strain in the polarization direction, S_{33}
- T_3 = contracted notation for the stress T_{33}
- D_3 = electric displacement in the polarization direction
- E_3 = electric field in the polarization direction
- F_{ST} = force exerted in the piezoelectric stack
- V = voltage
- d_{33} = contracted notation for the d_{333} piezoelectric coefficient
- s_{33} = contracted notation for the s_{3333} compliance coefficient
- ϵ_{33} = permittivity coefficient
- k_{ST} = stack stiffness
- k_{SP} = internal spring stiffness
- k_e = external stiffness
- F_0 = prestress force
- c = wave speed
- τ = time
- ρ = density
- η = elastic loss
- δ = dielectric loss
- γ = ratio ω/c
- λ = piezoelectric energy conversion loss
- i_{ST} = electric current

REFERENCES

- Ackerman, A. E., Liang, C. and Rogers, C. A. 1996. "Dynamic Transduction Characterization of Magnetostrictive Actuators," *Smart Materials and Structures*, 5(2):115–120.
- ANSI/IEEE 1987. *IEEE Standard on Piezoelectricity*, Std. 176, IEEE, New York.
- Brennan, M. C. and McGowan, A. M. 1997. "Piezoelectric Power Requirements for Active Vibration Control." In: *Proceedings on SPIE 4th Annual Symposium on Smart Structures and Materials: Mathematics and Control with Smart Structures*, Vol. 3039, pp. 660–669, 3–6 March, San Diego, CA.
- Chen, X., Fang, D. N. and Hwang, K. C. 1997. "Micromechanics Simulation of Ferroelectric Polarization Switching," *Acta Materialia*, 45(8):3181–3189.
- Ching-Yu Lin and Hagood, N. W. 2000. "Compression Depolarization of PZT Piezoelectric Materials under High Electromechanical Driving Levels." In: *Proceedings of SPIE Conference on Smart Structures and Materials 2000: Active Materials: Behavior and Mechanics*, Vol. 3992, pp. 114–125, Newport Beach, CA.

- Du, X., Belegundu, U. and Uchino, K. 1997. "Crystal Orientation Dependence of Piezoelectric Properties in Lead Zirconate Titanate: Theoretical Expectations for Thin Films," *Japanese Journal of Applied Physics*, Part 1, 37(9A):5580–5587.
- Fan, J, Stoll, W. A and Lynch, C. S. 1999. "Nonlinear Constitutive Behavior of Soft and Hard PZT: Experiments and Modeling," *Acta Materialia*, 47(17):4415–4425.
- Giurgiutiu, V., Chaudhry, Z. and Rogers, C. A. 1994. "The Analysis of Power Delivery Capability of Induced-Strain Actuators for Dynamic Applications." In: *Proceedings of the Second International Conference on Intelligent Materials, ICIM'94*, pp. 565–576, Colonial Williamsburg, VA.
- Giurgiutiu, V. and Rogers, C. A. 1996. "Power Energy Characteristics of Solid State Induced-Strain Actuators for Static and Dynamic Applications," *Journal of Intelligent Material Systems and Structure*, 7(6):656–667.
- Holland, R. 1967. "Representation of Dielectric, Elastic and Piezoelectric Losses by Complex Coefficients," *IEEE Transaction on Sonics and Ultrasonics*, SU-14(1):18–20.
- Huber, J. N. and Fleck, N. A. 2001. "Multi-Axial Electrical Switching of a Ferroelectric: Theory Versus Experiment," *Journal of Mechanics and Physics of Solids*, 49(4).
- Hwang, S. C. and McMeeking, R. M. 2000. "A Finite Element Model of Ferroelectric/Ferroelastic Polycrystals." In: *Proceedings on SPIE Conference on Smart Structures and Materials 2000: Active Materials: Behavior and Mechanics*, Vol. 3992, pp. 404–417, Newport Beach, CA.
- Ikeda, T. 1990. *Fundamentals of Piezoelectricity*, Oxford Science Publications, New York.
- Jordan, T., Ounaies, Z., Tripp, J. and Tchong, P. 2000. "Electrical Properties and Power Considerations of a Piezoelectric Actuator," NASA Technical Report NACA/CR-2000-209861.
- Kessler, H. and Balke, H. 2001. "On the Local and Average Energy Release in Polarization Switching Phenomena," *Journal of the Mechanics and Physics of Solids*, 49(5):953–978.
- Krueger, H. H. A. and Berlincourt, D. 1961. "Effects of High Static Stress on the Piezoelectric Properties of Transducer Materials," *The Journal of the Acoustical Society of America*, 33(10):1339–1344.
- Krueger, H. H. A. 1967. "Stress Sensitivity of Piezoelectric Ceramics: Part 1. Sensitivity to Compressive Stress Parallel to the Polar Axis," *The Journal of the Acoustical Society of America*, 42(3):636–645.
- Krueger, H. H. A. 1968. "Stress Sensitivity of Piezoelectric Ceramics: Part 3. Sensitivity to Compressive Stress Perpendicular to the Polar Axis," *Journal of the Acoustical Society of America*, 43(3):583–591.
- Lee, T. and Chopra, I. 1999. "Development and Validation of a Refined Piezostack-Actuated Trailing Edge Flap Actuator for a Helicopter Rotor." In: *Proceedings on SPIE Conference on Smart Structures and Integrated Systems*, Vol. 3668, pp. 22–36, Newport Beach, CA.
- Liang, C., Sun, F. P. and Rogers, C. A. 1994. "Coupled Electro-Mechanical Analysis of Adaptive Material Systems – Determination of the Actuator Power Consumption and System Energy Transfer," *Journal of Intelligent Material Systems and Structures*, 5(1):12–20.
- Lin, C.-Y. and Hagoood, N. W. 2000. "Compression Depolarization of PZT Piezoelectric Materials Under High Electromechanical Driving Levels." In: *Proceedings SPIE Conference on Smart Structures and Materials*, Vol. 3992, pp. 115–125, Newport Beach, CA.
- Lynch, C. S. 1996. "The Effect of Uniaxial Stress on the Electro-Mechanical Response of 8/65/35 PLZT," *Acta Materialia*, 44(10):4137–4148.
- Maxwell, J. K. 1954. *A Treatise on Electricity and Magnetism*, Vol. 1, Dover Publications, Inc., New York.
- Mitrovic, M., Carman, G. P. and Straub, F. K. 1999. "Electromechanical Characterization of Piezoelectric Stack Actuators." In: *Proceedings on SPIE Conference on Smart Structures and Integrated Systems*, Vol. 3668, pp. 586–601, Newport Beach, CA.
- Mitrovic, M., Carman, G. P. and Straub, F. K. 2000. "Durability Characterization of Piezoelectric Stack Actuators Under Combined Electro-Mechanical Loading," *41st AIAA/ASME/ASCE/AHS/ASC Conference Structures, Structural Dynamics, and Materials*, Paper No. AIAA 2000-1500, Atlanta, GA.
- Pan, M.-J., Rehrig, P. W., Kucera, J. P., Park, S.-E. and Hackenberger, W. S. 2000. "Comparison of Actuator Properties for Piezoelectric and Electrostrictive Materials." In: *Proceedings SPIE Conference on Smart Structures and Materials*, Vol. 3992, pp. 80–90, Newport Beach, CA.
- Pomirleanu 2001. "Induced Strain Actuators for Smart-Structures Applications," M.S. Thesis, University of South Carolina, Mechanical Engineering Department, Columbia SC.
- Straub, F. K. and Merkley, D. J. 1995. "Design of a Smart Material Actuator for Rotor Control," *1995 SPIE North American Conference on Smart Structures and Materials, Smart Structures and Integrated Systems*, Paper No. 2443-10, San Diego, CA.
- Straub, F. K., Ngo, H. T. and Domzalski, D. B. 1999. "Development of a Piezoelectric Actuator for Trailing Edge Flap Control of Rotor Blades." In: *Proceedings on SPIE Conference on Smart Structures and Integrated Systems*, Vol. 3668, pp. 2–13, Newport Beach, CA.
- Uchino, K. 2000. *Ferroelectric Devices*, Marcel Dekker Inc., New York.
- Yang, G., Liu, S.-F., Ren, W. and Mukerjee, B. K. 2000. "Uniaxial Stress Dependence of the Piezoelectric Properties of Lead Zirconate Titanate Ceramics." In: *Proceedings on SPIE Conference on Smart Structures and Materials 2000: Active Materials: Behavior and Mechanics*, Vol. 3992, pp. 103–113, Newport Beach, CA.
- Zhang, Q. M., Zhao, J., Uchino, K. and Zheng, J. 1997. "Change of Weak-Field Properties of $\text{Pb}(\text{ZrTi})\text{O}_3$ Piezoceramics with Compressive Uniaxial Stresses and Its Links to the Effect of Dopants on the Stability of the Polarizations in the Materials," *Journal of Material Research*, 12(1):226–234.